

Article

Crystalline Phase, Cross-Section, and Temporal Characteristics of Erbium-Ion in Lu₃Ga₅O₁₂ Crystal

Pei Zhang ^{1,2}, De-Long Zhang ^{2,*}  and Yan Wang ^{3,*}

¹ School of Mechanical Engineering, Tianjin Sino-German University of Applied Sciences, 2 Yanshan Rd, Haihe Education Park, Tianjin 300350, China; princezhangpei@163.com

² School of Precision Instruments and Opto-Electronics Engineering, and with Key Lab of Optoelectronic Information Technology (Ministry of Education), and Key Lab of Micro-Opto-Electro-Mechanical Systems (MOEMS) Technology (Ministry of Education), Tianjin University, Tianjin 300072, China

³ Fujian Institute of Research on the Structure of Matter, Chinese Academy of Sciences, Fuzhou 350002, China

* Correspondence: dlzhang@tju.edu.cn (D.-L.Z.); wy@fjirsm.ac.cn (Y.W.)

Abstract: An erbium-doped Lu₃Ga₅O₁₂(LuGG) single crystal was grown by the Czochralski method. The crystalline phase in the grown crystal was analyzed by powder X-ray diffraction. The erbium-ion emission spectra of the crystal were acquired. The erbium-ion emission cross-section (ECS) spectrum was computed from the acquired emission spectrum. The erbium-ion absorption cross-section (ACS) spectrum was computed using the McCumber relationship. The results are discussed in contrast to those computed from the acquired absorption spectrum, and the comparison shows that both methods give consistent results. The temporal characteristics of the emissions were also studied based on 0.98 μm pulse pumping. The study shows that the infrared emissions at 1.0, 1.5, and 2.8 μm show mono-exponentially temporal behavior. Instead, the decays of two visible emissions at 0.56 and 0.67 μm show considerable non-exponential features; each trace can be fitted double-exponentially. The non-exponential behavior is associated with those erbium ions that are present in the form of clusters, which enables non-radiative upconversion depopulation and hence additional contribution to the decay through cross relaxation between the erbium ions in clusters. The study also shows that about half of the erbium ions are present in the cluster state in the studied crystal.

Keywords: Er³⁺-doped LuGG single crystal; emission/absorption cross section; temporal decaying feature



Citation: Zhang, P.; Zhang, D.-L.; Wang, Y. Crystalline Phase,

Cross-Section, and Temporal

Characteristics of Erbium-Ion in

Lu₃Ga₅O₁₂ Crystal. *Photonics* **2023**,

10, 586. [https://doi.org/10.3390/](https://doi.org/10.3390/photronics10050586)

[photronics10050586](https://doi.org/10.3390/photronics10050586)

Received: 29 March 2023

Revised: 13 May 2023

Accepted: 15 May 2023

Published: 17 May 2023



Copyright: © 2023 by the authors. Licensee MDPI, Basel, Switzerland. This article is an open access article distributed under the terms and conditions of the Creative Commons Attribution (CC BY) license (<https://creativecommons.org/licenses/by/4.0/>).

1. Introduction

Garnet is isotropic, belongs to a cubic system with a space group of *Ia-3d* (O_h¹⁰), and has been widely studied because of its attractive merits, such as higher stability in structure, mechanics, and chemistry; better thermal conductivity; lower lattice vibrational frequency; larger solidity; a broader range of transparency; easier growth of a high-quality crystal with a larger size; and a larger admittance of lanthanide ions in its lattice. A lanthanide-doped garnet enables the merging of all of these merits and photo-luminescence characteristics of lanthanide ions and is promising for uses in display, laser, and thermal sensing on the basis of fluorescence intensity ratio (FIR).

Garnet has the common molecular formula α₃β₂γ₃O₁₂ with (α = Lu, Gd, Y), (β = Ga, Al, Sc, Fe), and (γ = Ga, Al, Fe). It can be classified into three kinds of garnets on the basis of different γ atoms, i.e., iron-based garnet such as YIG (Y₃Fe₅O₁₂), Al-based garnet such as YAG (Y₃Al₅O₁₂), and gallium-based garnet, e.g., Gd₃Ga₅O₁₂ and Lu₃Ga₅O₁₂ (LuGG). Lanthanide-doped LuGG has all the advantages of a lanthanide-doped garnet. In recent years, studies have been performed on several lanthanide-/transition metal-doped LuGG single crystals or polycrystalline powders. The dopants concern the ions erbium [1–5], ytterbium [5–10], chromium [11], samarium [12], holmium [13], neodymium [14], and bismuth [15].

For the erbium-doped LuGG, preliminary spectroscopic studies have been performed on its single-crystal [1,2] and polycrystalline powder states [3–5], and the results show that the material is promising for implementation of an infrared laser or thermal sensor on the basis of FIR of 0.98- μm -excited 0.53 and 0.56 μm fluorescence. Both the longer lifetime ($\sim 500 \mu\text{s}$) of the $^4I_{11/2}$ ($\sim 1.0 \mu\text{m}$) level of erbium-ion in the LuGG crystal as given below (it is only 220 μs for Er^{3+} -doped LiNbO_3 crystal [16]) and the lower lattice vibrational frequency (766 cm^{-1}) [2] favor the 0.98- μm -excited emissions [for inorganic materials, maximum phonon frequency usually ranges from $\sim 200 \text{ cm}^{-1}$ (e.g., fluorides) to $\sim 1500 \text{ cm}^{-1}$ (such as borates)]. In particular, lasing at 2.8 μm has been demonstrated previously [1].

Entire spectroscopic data are necessary for the design and optimization of a laser or thermal sensor based on such a potential active material. Following an earlier Judd-Ofelt study and luminescence features [1,2], the present work aims at cross-section spectrum properties of erbium-doped LuGG in single-crystal state, which are basic spectral data and were not yet reported previously. First, near-infrared (NIR), mid-infrared (mid-IR), and visible (Vis) emission spectra of erbium-doped LuGG crystals have been acquired. Second, erbium-ion emission cross-section (ECS) spectra are computed on the basis of the acquired emission spectra. Third, the absorption cross-section (ACS) spectra are derived from two approaches. One is to use the McCumber relationship, and another is to employ the acquired absorption spectrum. A comparison is made between the results given by the two approaches. Finally, temporal features of the luminescence of the erbium ion in the studied crystal have been studied under 0.98 μm pulse excitation.

2. Experiment

The erbium-doped LuGG single crystal employed in this work was pulled by the Czochralski method. Initial materials include lutetium oxide (99.99%), gallium oxide (99.99%), and erbium oxide (99.99%). During growth, the pulling rate is similar to 1.0–1.2 mm per hour, and the rotation speed is 8–12 rounds per minute. The concentrations of erbium, lutetium, and gallium ions in the solid were given by carrying out the ICP-AES analysis, which has a relative error of 10%. The analysis gave a lutetium concentration of $(10.3 \pm 1.1) \times 10^{21} \text{ ions/cm}^3$, an erbium concentration of $(2.6 \pm 0.3) \times 10^{21} \text{ ions/cm}^3$ [$\sim 20 \text{ at}\% = C_{\text{Er}}/(C_{\text{Er}} + C_{\text{Lu}})$], and a gallium concentration of $(21.5 \pm 2.2) \times 10^{21} \text{ ions/cm}^3$.

By making use of a spectrometer (U-4100), optical absorption of erbium ions in a $1.12 \pm 0.01 \text{ mm}$ thick LuGG single-crystal plate was investigated in the wavelength range of 300–1700 nm in the case of a 1.0 nm scanning step and a 300 nm/min speed.

Vis and NIR fluorescence spectra of the erbium-doped LuGG crystal were acquired using an Edinburgh FLS980 spectrometer. Either an external continuous-wave 0.98 μm laser diode or an xenon lamp (450 W) was adopted as the pumping source. The spectra of the transitions at 0.53, 0.56, 0.67, and 1.5 μm were acquired using an external 0.98 μm laser diode as the pumping source, and that of the transition at 1.0 μm was acquired using 0.52 μm output from the xenon lamp as the pumping source. The spectrum of the transition at mid-IR ($\sim 2.8 \mu\text{m}$) was acquired by an Edinburgh FSP920-C spectrometer, and the excitation source adopted was a 0.98 μm output from a tunable OPO nanosecond pulse laser. Figure 1 depicts erbium-ion energy levels, together with the main processes under the 0.98 μm wavelength pumping, including the NIR transition at 1.5, the mid-IR transition at 2.8 μm , and the Vis transitions at 0.53, 0.56, and 0.67 μm , mainly due to cooperative upconversion (CU) and excited state absorption (ESA).

The temporal decaying characteristics of the erbium-ion fluorescence in the LuGG single crystal under study were investigated using the Edinburgh FLS980 spectrometer for the Vis and NIR transitions and the Edinburgh FSP920-C spectrometer for the mid-IR transition. The Vis and mid-IR fluorescence was excited using the above-mentioned nanosecond pulse laser. The NIR fluorescence at 1.0 and 1.5 μm was excited by microsecond pulses emitted from a flash lamp.

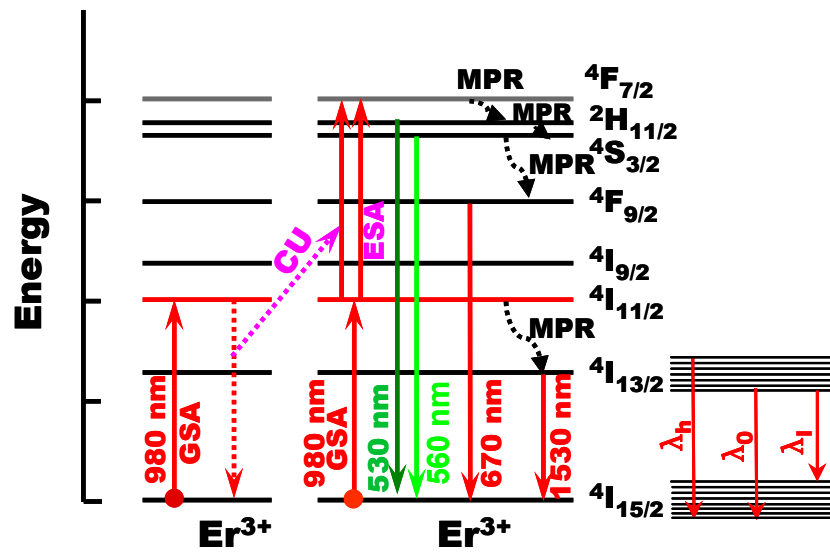


Figure 1. Left part: erbium-ion energy levels and main processes under the 0.98 μm wavelength pumping. CU: cooperative upconversion, ESA: excited state absorption; GSA: ground state absorption; MPR: multi-phonon relaxation. Right part: extreme processes between Stark splittings of $^4I_{13/2}$ and $^4I_{15/2}$. λ_0 : peaking wavelength of transition from the lowest sublevel of the $^4I_{13/2}$ state to that of the $^4I_{15/2}$ state; λ_h (λ_l): wavelength that satisfies the five-percentage rule in the high (low) energy region.

3. Results and Discussion

3.1. X-ray Diffraction and Crystalline Phase

The crystalline phase of the grown crystal was analyzed by powder X-ray diffraction (Rigaku D/MAX 2500). Figure 2 shows the measured pattern of the grown crystal (see the upper one). For reference purposes, the pattern of undoped LuGG crystal is also given in the lower part, and the pattern is drawn on the basis of powder diffraction file (PDF) #73-1372. All discernible reflexes are indexed. We can see that the two patterns are almost identical except for an alteration in relative intensity. It is therefore concluded that the crystal grown by us is dominated by the LuGG crystalline phase.

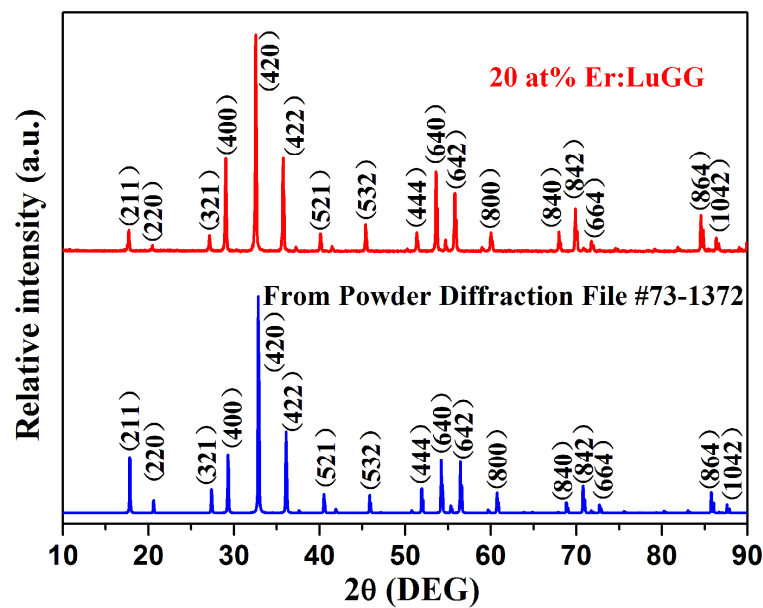


Figure 2. XRD patterns of the studied crystal (upper) and pure LuGG taken from powder diffraction file 73-1372 (down). All discernible reflexes are indexed.

We note that, although the erbium-doped LuGG crystal has an erbium concentration as high as 20 at%, its X-ray diffraction pattern does not reveal a noticeable difference from that of the undoped crystal. This is due to the larger admittance of lanthanide ions in the lattice of a garnet, as mentioned in the introduction. The argument is verified by the fact that the Er^{3+} ion in the $\text{Lu}_3\text{Ga}_5\text{O}_{12}$ single crystal has a segregation coefficient of ~ 1.0 . This is because Er^{3+} and Lu^{3+} ions have close ionic radii: 0.881 Å for Er^{3+} and 0.848 Å for Lu^{3+} , which cause less mismatch in the lattice. A segregation coefficient of ~ 1.0 means that the Er^{3+} concentration in the grown crystal has good uniformity, and hence the $\text{Lu}_3\text{Ga}_5\text{O}_{12}$ has excellent admitting capability of Er^{3+} and is a good host material for Er^{3+} dopants.

3.2. Er^{3+} Emission Characteristics and 980 nm Upconversion Mechanism

Figure 3a–d shows the measured emission spectra of the electronic transitions ${}^2\text{H}_{11/2} \leftrightarrow {}^4\text{S}_{3/2}$ (530 nm), ${}^4\text{S}_{3/2} \leftrightarrow {}^4\text{I}_{15/2}$ (560 nm), ${}^4\text{F}_{9/2} \leftrightarrow {}^4\text{I}_{15/2}$ (670 nm), ${}^4\text{I}_{11/2} \leftrightarrow {}^4\text{I}_{15/2}$ (1020 nm), and ${}^4\text{I}_{13/2} \leftrightarrow {}^4\text{I}_{15/2}$ (1530 nm) of erbium ions in the LuGG crystal. Figure 3e shows the spectrum of the mid-infrared emission at 2.8 μm , which involves a transition between two intermediate states, ${}^4\text{I}_{11/2}$ and ${}^4\text{I}_{13/2}$. The main emission peaks are indicated for each transition. The spectra of visible emissions at 530, 560, and 670 nm were recorded under the 980 nm wavelength excitation. These spectra originate from upconversion emissions. For the two green emissions, the spectral region of < 535 nm concerns the transition ${}^2\text{H}_{11/2} \leftrightarrow {}^4\text{I}_{15/2}$ and that of > 535 nm involves the ${}^4\text{S}_{3/2} \leftrightarrow {}^4\text{I}_{15/2}$ transition. The most remarkable feature of the three visible upconversion emissions is that the red emission has a maximum intensity nearly four times larger than the green emission at 560 nm, and the 560 nm emission has a maximum intensity approximately one order of magnitude larger than another green emission at 530 nm, as shown in Figure 3a,b, which were recorded under the completely same experimental condition. For the two near-infrared emissions, typical Er^{3+} emission spectra were recorded at the 1.0 and 1.5 μm regions. The potential lasing wavelengths there include 1023, 1531, 1568, 1620, and 1642 nm. At the 2.8 μm spectral region, three peaking emissions at 2635, 2710, and 2815 nm could be resolved, as shown in Figure 3e. Among them, lasing at the latter two wavelengths has been demonstrated [1].

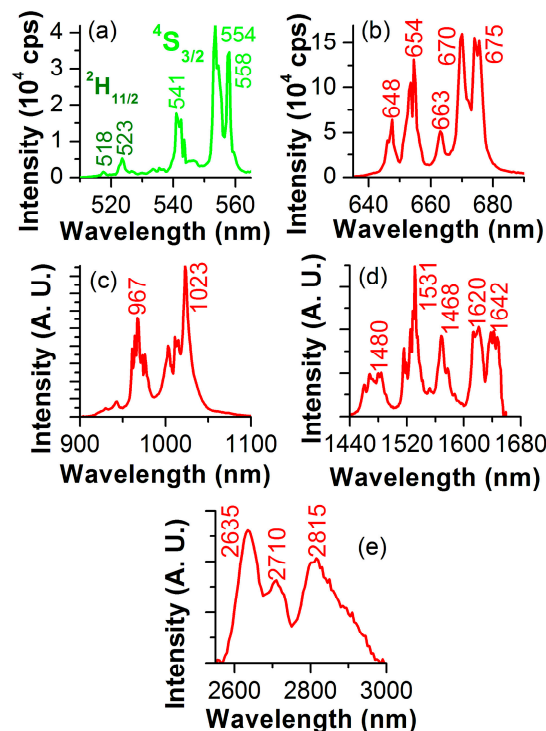


Figure 3. Vis (a,b), NIR (c,d), and mid-IR (e) emission spectra of an erbium (20 at%)-doped LuGG crystal. Peaking emission wavelengths are indicated for each transition.

To understand the upconversion mechanism, the upconversion emission intensity (I_{UC}) was measured as a function of the density of pumping power (I_p). The upconversion emission intensity I_{UC} and the pump power I_p obey the following power relationship: $I_{UC} \propto (I_p)^n$, where n is the power index that determines the number of photons required to realize a specific radiative transition. The integrated intensity of each emission band on the logarithmic scale, $\ln(I_{UC})$, is calculated and plotted against the 980 nm excitation beam intensity on the logarithmic scale, $\ln(I_p)$. The results are shown in Figure 4. The green balls concern the two green emissions ${}^2H_{11/2} \leftrightarrow (530 \text{ nm})$ and ${}^4S_{3/2} \leftrightarrow {}^4I_{15/2}$ (560 nm), and the red balls involve the red emission ${}^4F_{9/2} \leftrightarrow {}^4I_{15/2}$ (670 nm). A linear fit was performed on each plot, and the slope obtained from the linear fit yields the value of the power index n . The resultant n values are indicated in Figure 4. Good fitting is obtained for each case. The fits give the same n value of 1.77 for both the green and red emissions. The n value suggests that the two-photon process is the dominant mechanism for the 980 nm upconversion emissions of the erbium-doped LuGG crystal studied here. The two-photon process responsible for the upconversion emissions concerns the CU and ESA, as indicated in Figure 1. As demonstrated below, the energy transfer CU process would be more likely for the excitation of the ${}^2H_{11/2}$ and ${}^4S_{3/2}$ states in the highly erbium-doped LuGG crystal studied here.

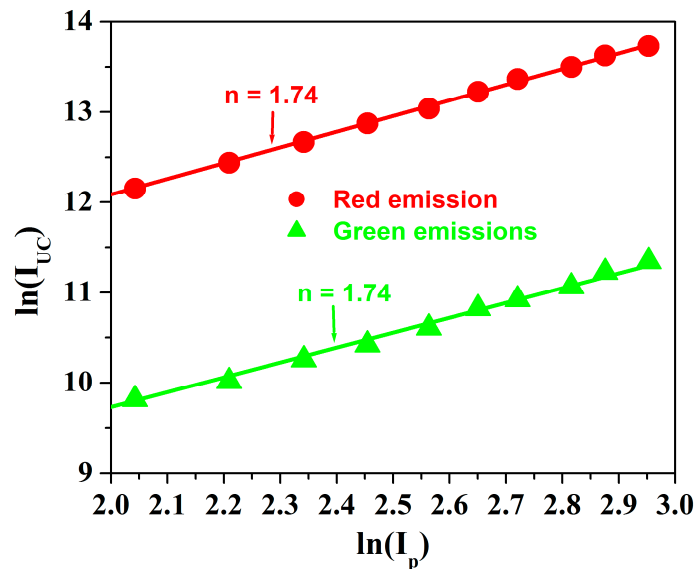


Figure 4. Integrated upconversion fluorescence intensity I_{UC} as a function of 980 nm pump intensity I_p on a logarithmic scale for erbium(20 at%)-doped LuGG crystal. Red balls: red emission ${}^4F_{9/2} \leftrightarrow {}^4I_{15/2}$ (670 nm); green balls: green emissions: ${}^2H_{11/2} \leftrightarrow (530 \text{ nm}) + {}^4S_{3/2} \leftrightarrow {}^4I_{15/2}$ (560 nm).

3.3. ECS and ACS Spectra of Erbium-Ion in LuGG Crystal

From the acquired emission intensity at wavelength λ , named $\xi(\lambda)$, erbium-ion ECS, named $\Sigma_e(\lambda)$, can be evaluated using the following equation [17–22]:

$$\Sigma_e(\lambda) = \frac{P_{rad}\lambda^5\xi(\lambda)}{8\pi c \int_{band} (RI)^2(\lambda)\xi(\lambda)\lambda d\lambda} \tag{1}$$

where λ and c are wavelength and light velocity in vacuum, respectively; $RI(\lambda)$ is the λ -related index of refraction of matrix material; and P_{rad} is the radiative rate of the transition concerned. The integral in Equation (1) is calculated over the entire emission band. For the two transitions ${}^2H_{11/2} \leftrightarrow {}^4I_{15/2}$ and ${}^4S_{3/2} \leftrightarrow {}^4I_{15/2}$, which are thermalized and hypersensitive, P_{rad} denotes an effective radiative rate [23].

Based on the calculated $\Sigma_e(\lambda)$, we can compute the corresponding ACS, named $\Sigma_a(\lambda)$, with the aid of the McCumber expression [21,22]:

$$\Sigma_a(\lambda) = \Sigma_e(\lambda) \exp\left(\frac{E - E_E}{k_B T}\right) \quad (2)$$

where k_B is the Boltzmann constant, $E = hc/\lambda$, and E_E is the excitation energy of a given transition [23]. For ${}^2H_{11/2} \leftrightarrow {}^4I_{15/2}$ and ${}^4S_{3/2} \leftrightarrow {}^4I_{15/2}$, E_E denotes an effective excitation energy [23].

The ACS $\Sigma_a(\lambda)$ can also be obtained directly from the measured absorption spectrum on the basis of Beer-Lambert law.

$$\Sigma_a(\lambda) = k(\lambda)/C_A \quad (3)$$

where $k(\lambda)$ is the absorption coefficient and C_A is the concentration of active ions (erbium ions).

It can be seen from Equation (2) that the E_E is a crucial parameter that needs to be evaluated first. To achieve it, some relevant energy level parameters should be computed. Particularly for the green transition processes ${}^4S_{3/2} \leftrightarrow {}^4I_{15/2}$ and ${}^2H_{11/2} \leftrightarrow {}^4I_{15/2}$, five parameters are needed that include the Stark splittings δG_k ($k = G, L,$ and U) of the ground state ${}^4I_{15/2}$ (G), lower state ${}^4S_{3/2}$ (L), and upper level ${}^2H_{11/2}$ (U) manifolds, and the interval either between the ${}^4I_{15/2}$ and ${}^4S_{3/2}$ states, named δG_{LG} , or between ${}^2H_{11/2}$ and ${}^4S_{3/2}$ states, named δG_{UL} . For other red, NIR, and mid-IR transition processes, the parameters required include the energy splittings of two relevant manifolds and their intervals. A five-percentage rule in combination with discrimination of peaking fluorescence related to the extreme transition has been used to compute these input parameters [23–25]. It is assumed in the computation that each manifold involved has identical Stark splittings. Next, we exemplify the ${}^4I_{13/2} \leftrightarrow {}^4I_{15/2}$ (1.5 μm) transition to detail the computation procedure. It is evident that the well-known fluorescence peak at $\lambda_0 = 1.531 \mu\text{m}$ is assigned to the transition process from the lowest Stark level of ${}^4I_{13/2}$ (U) to that of the ground state of ${}^4I_{15/2}$ (L) [23–25]. The gap between the two states is then estimated as $\delta G_{UL} = 6531.7 \pm 2.1 \text{ cm}^{-1}$. Next, the emission bandwidth of the transition is estimated on the basis of the five-percentage rule [23–25]. The rule is fulfilled for $\lambda_l = 1.655 \mu\text{m}$ in the low-energy region and $\lambda_h = 1.454 \mu\text{m}$ in the high-energy region (in the right part of Figure 1, we have marked the wavelengths (λ_0 , λ_h , and λ_l)). On the basis of the values of λ_0 , λ_h , and λ_l , we have the Stark splittings $\delta G_L = 69.4 \pm 0.6 \text{ cm}^{-1}$ and $\delta G_U = 57.7 \pm 0.7 \text{ cm}^{-1}$. Finally, one can compute the excitation energy E_E or $\lambda_E = hc/E_E = 1534.8 \pm 0.7 \text{ nm}$. Similarly, one can compute the energy parameters and E_E or λ_E of other transition processes, including the effective P_{rad} and E_E or λ_E of the two green processes ${}^4I_{15/2} \leftrightarrow {}^4S_{3/2}$ and ${}^4I_{15/2} \leftrightarrow {}^2H_{11/2}$. Table 1 summarizes the computed values of the parameters.

Based on the emission spectra shown in Figure 3a–d, we have computed using Equations (1) and (2) the ECS (red) and ACS (green) spectra of the transition processes ${}^4I_{15/2} \leftrightarrow {}^4S_{3/2}$ (0.56 μm), ${}^4I_{15/2} \leftrightarrow {}^2H_{11/2}$ (0.53 μm), ${}^4I_{15/2} \leftrightarrow {}^4F_{9/2}$ (0.67 μm), ${}^4I_{15/2} \leftrightarrow {}^4I_{11/2}$ (1.0 μm), and ${}^4I_{15/2} \leftrightarrow {}^4I_{13/2}$ (1.5 μm) of erbium-ion in the LuGG crystal. The calculated results are shown in Figure 5. Due to the linearity between the ECS $\Sigma_e(\lambda)$ and the emission intensity $\xi(\lambda)$ as shown in Equation (1), each ECS spectrum in Figure 5 has little difference from the corresponding emission spectrum shown in Figure 3. The ECS error originates predominantly from the uncertainty of P_{rad} . Juud-Ofelt analysis yielded a relative uncertainty of 18.1%, 13.7%, and 13.4% for the radiative transitions ${}^4F_{9/2} \leftrightarrow {}^4I_{15/2}$ (0.67 μm), ${}^4I_{11/2} \leftrightarrow {}^4I_{15/2}$ (1.0 μm), and ${}^4I_{13/2} \leftrightarrow {}^4I_{15/2}$ (1.5 μm), respectively, and an effective error percentage of 14.4% for the two processes ${}^2H_{11/2} \leftrightarrow {}^4I_{15/2}$ and ${}^4S_{3/2} \leftrightarrow {}^4I_{15/2}$ [2]. The uncertainties of ACS $\Sigma_a(\lambda)$ can be computed from the known incertitude of $\Sigma_e(\lambda)$ and E_E on the basis of Equation (2). The uncertainty percentage is given by

$$\frac{\Delta \Sigma_a}{\Sigma_a} = \frac{\Delta \Sigma_e}{\Sigma_e} + \frac{E_E}{k_B T} \frac{\Delta E_E}{E_E} = \frac{\Delta \Sigma_e}{\Sigma_e} + \frac{E_E}{k_B T} \frac{\Delta \lambda_E}{\lambda_E} \quad (4)$$

Table 1. Values of parameters for computation of the ECS and ACS spectra of erbium-doped LuGG.

Band at	Parameter	Value	Band at	Parameter	Value
0.53 μm ($^2\text{H}_{11/2}$) + 0.56 μm ($^4\text{S}_{3/2}$) G: $^4\text{I}_{15/2}$ L: $^4\text{S}_{3/2}$ U: $^2\text{H}_{11/2}$	P_{HG} (s^{-1})	2785.9 ± 563.7	0.65 μm L: $^4\text{I}_{15/2}$ U: $^4\text{F}_{9/2}$	P_{rad} (s^{-1})	1760.4 ± 318.8
	P_{SG} (s^{-1})	3340.9 ± 471.4		$\lambda_{\text{h}}/\lambda_0/\lambda_{\text{l}}$ (nm)	643.5/663/683
	$\lambda_{\text{h}}/\lambda_0/\lambda_{\text{l}}$ (nm)	517.5/523.5/537		δG_{UL} (cm^{-1})	$15,083.0 \pm 4.5$
	$\lambda_{\text{h}}/\lambda_0/\lambda_{\text{l}}$ (nm)	541/546.5/559.5		δG_{U} (cm^{-1})	114.2 ± 5.9
	δG_{UL} (cm^{-1})	803.9 ± 35.0		δG_{L} (cm^{-1})	63.1 ± 3.2
	δG_{LG} (cm^{-1})	$18,298.3 \pm 6.7$		λ_{E} (nm)	653.0 ± 0.7
	δG_{G} (cm^{-1})	64.6 ± 5.8		P_{rad} (s^{-1})	341.5 ± 47.2
	δG_{U} (cm^{-1})	44.3 ± 5.3		$\lambda_{\text{h}}/\lambda_0/\lambda_{\text{l}}$ (nm)	961/976/1023
	δG_{L} (cm^{-1})	186.0 ± 33.8		δG_{UL} (cm^{-1})	$10,245.9 \pm 5.2$
	P_{rad} (s^{-1})	3311.2 ± 476.8		δG_{U} (cm^{-1})	31.9 ± 2.1
1.53 μm L: $^4\text{I}_{15/2}$ U: $^4\text{I}_{13/2}$	λ_{E} (nm)	532.2 ± 0.4	0.98 μm L: $^4\text{I}_{15/2}$ U: $^4\text{I}_{11/2}$	δG_{L} (cm^{-1})	67.2 ± 1.4
	P_{rad} (s^{-1})	354.3 ± 47.5		λ_{E} (nm)	980.6 ± 0.8
	$\lambda_{\text{h}}/\lambda_0/\lambda_{\text{l}}$ (nm)	1454/1531/1655		P_{rad} (s^{-1})	59.4 ± 8.0
	δG_{UL} (cm^{-1})	6531.7 ± 2.1		$\lambda_{\text{h}}/\lambda_0/\lambda_{\text{l}}$ (nm)	2576/2700/2969
	δG_{U} (cm^{-1})	57.7 ± 0.7		δG_{UL} (cm^{-1})	3714.2 ± 1.5
	δG_{L} (cm^{-1})	69.4 ± 0.6		δG_{U} (cm^{-1})	31.9 ± 2.1
2.8 μm L: $^4\text{I}_{13/2}$ U: $^4\text{I}_{11/2}$	λ_{E} (nm)	1534.8 ± 0.7	2.8 μm L: $^4\text{I}_{13/2}$ U: $^4\text{I}_{11/2}$	δG_{L} (cm^{-1})	57.7 ± 0.7
	P_{rad} (s^{-1})	354.3 ± 47.5		λ_{E} (nm)	2719.7 ± 5.0
	$\lambda_{\text{h}}/\lambda_0/\lambda_{\text{l}}$ (nm)	1454/1531/1655		P_{rad} (s^{-1})	59.4 ± 8.0
	δG_{UL} (cm^{-1})	6531.7 ± 2.1		$\lambda_{\text{h}}/\lambda_0/\lambda_{\text{l}}$ (nm)	2576/2700/2969
	δG_{U} (cm^{-1})	57.7 ± 0.7		δG_{UL} (cm^{-1})	3714.2 ± 1.5

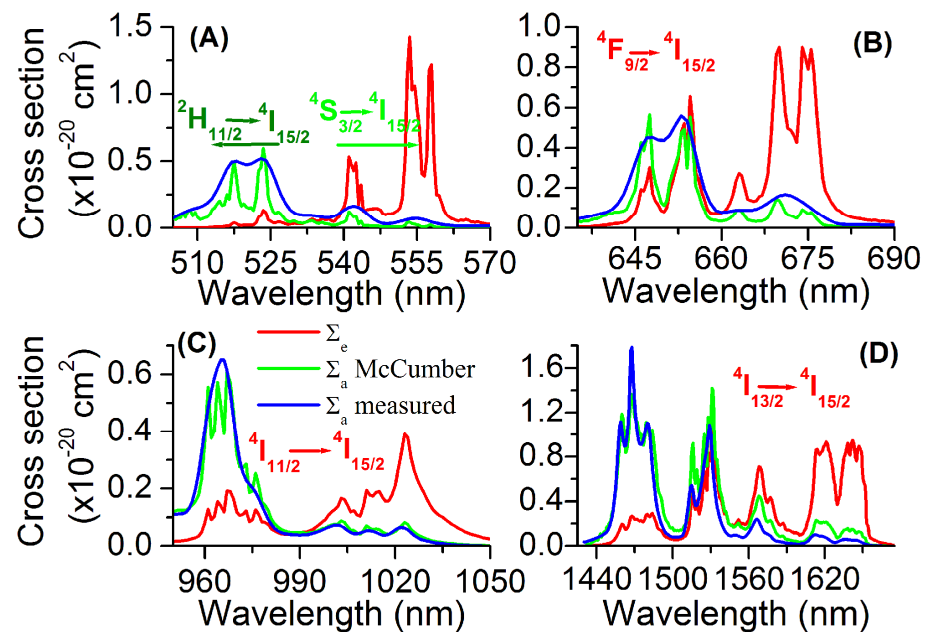


Figure 5. Vis and NIR ECS (red curve) and deduced ACS (green curve) spectra of (A) $^2\text{H}_{11/2} \leftrightarrow ^4\text{I}_{15/2}$ and $^4\text{S}_{3/2} \leftrightarrow ^4\text{I}_{15/2}$, (B) $^4\text{F}_{9/2} \leftrightarrow ^4\text{I}_{15/2}$, (C) $^4\text{I}_{11/2} \leftrightarrow ^4\text{I}_{15/2}$, and (D) $^4\text{I}_{13/2} \leftrightarrow ^4\text{I}_{15/2}$ of erbium(20 at%)-doped LuGG. The ACS spectrum (blue curve) computed from the measured absorption spectrum is also presented.

It is about 26.0%, 19.9%, and 14.8% for the $^4\text{I}_{15/2} \leftrightarrow ^4\text{F}_{9/2}$ (0.67 μm), $^4\text{I}_{15/2} \leftrightarrow ^4\text{I}_{11/2}$ (1.0 μm), and $^4\text{I}_{15/2} \leftrightarrow ^4\text{I}_{13/2}$ (1.5 μm), respectively, and 21.2% for the $^4\text{I}_{15/2} \leftrightarrow ^4\text{S}_{3/2}$ (0.56 μm) and $^4\text{I}_{15/2} \leftrightarrow ^2\text{H}_{11/2}$ (0.53 μm).

Figure 5 also shows the ACS spectrum obtained from the measured absorption spectrum (blue plots) for each transition. Its uncertainty percentage is similar to 16%, contributed by the experimental error of erbium-ion concentration, ~15%, and that of sample thickness, ~1%, in the absorption measurement. Table 2 collects the values of some ECS and ACS peaks of typical transition processes. One can see that the ACS data computed from the McCumber relation can be thought of as the same as those computed from the measured absorption spectrum within the uncertainty. The consistency gives a hint that both methods are correct, and the ACS result obtained from either of them is sound.

Table 2. Peaking values of ECS (Σ_e) and ACS Σ_a ($\times 10^{-20} \text{ cm}^2$) of typical transitions of erbium-ion in LuGG. The ACS values obtained from the measured absorption spectrum are also presented.

Erbium-Ion Transitions	$\Sigma_e@ \lambda$ ($\times 10^{-20} \text{ cm}^2$)	$\Sigma_a@ \lambda \text{ nm}$ ($\times 10^{-20} \text{ cm}^2$)	
		McCumber	Absorption Spectrum
$^4I_{15/2} \leftrightarrow ^4I_{13/2}$	0.27@1468 nm	1.36@1468 nm	1.79@1468 nm
	1.20@1531 nm	1.42@1531 nm	1.09@1531 nm
$^4I_{11/2} \leftrightarrow ^4I_{13/2}$	0.47@2635 nm	0.84@2635 nm	-
	0.53@2815 nm	0.29@2815 nm	-
$^4I_{15/2} \leftrightarrow ^4I_{11/2}$	0.19@967 nm	0.61@967 nm	0.65@967 nm
	0.39@1023 nm	0.08@1023 nm	0.07@1023 nm
$^4I_{15/2} \leftrightarrow ^4F_{9/2}$	0.30@648 nm	0.56@648 nm	0.45@648 nm
	0.65@655 nm	0.55@655 nm	0.53@655 nm
	0.90@670 nm	0.14@670 nm	0.16@670 nm
	0.90@674 nm	0.09@674 nm	0.13@674 nm
$^4I_{15/2} \leftrightarrow ^4S_{3/2}$	0.53@541 nm	0.13@541 nm	0.15@541 nm
	1.43@554 nm	0.05@554 nm	0.07@554 nm
	1.22@558 nm	0.03@558 nm	0.04@558 nm
$^4I_{15/2} \leftrightarrow ^2H_{11/2}$	0.04@518 nm	0.50@518 nm	0.50@518 nm
	0.13@524 nm	0.60@524 nm	0.52@524 nm

In respect to the mid-IR transition at $\sim 2.8 \mu\text{m}$, $^4I_{11/2} \leftrightarrow ^4I_{13/2}$, the process concerns two intermediate manifolds. One cannot get its absorption features as readily as those of a conventional ground-state absorption transition. Its ACS must be computed from the measured fluorescence spectrum on the basis of the McCumber relation. Figure 6 illustrates the computed ECS and ACS spectra of the transition. In particular, the ECS/ACS has a value of $0.47/0.84 \times 10^{-20} \text{ cm}^2$ at $2.635 \mu\text{m}$ and $0.53/0.29 \times 10^{-20} \text{ cm}^2$ at $2.815 \mu\text{m}$. These ECS/ACS values, as input parameters, can be used to design an efficient mid-infrared laser operated at either 2.635 or $2.815 \mu\text{m}$ on the basis of population inversion: $\Sigma_e(\lambda)N_U - \Sigma_a(\lambda)N_L$, where N_U and N_L represent the populations of the upper state ($^4I_{11/2}$) and lower state ($^4I_{13/2}$), respectively. As the gain coefficient is proportional to the population inversion, an efficient laser is more easily achieved for the emission at $2.815 \mu\text{m}$ because its ECS value, $0.53 \times 10^{-20} \text{ cm}^2$, is nearly two times the corresponding ACS value, $0.29 \times 10^{-20} \text{ cm}^2$.

3.4. Temporal Characteristics

Aiming at the fluorescence peaks at 0.554 , 0.67 , 1.023 , 1.531 , and $2.815 \mu\text{m}$, we have measured their temporal traces, obtained their lifetimes, and studied their temporal decaying characteristics. Figure 7 shows the measured transient decay curves of the three infrared emissions at (a) 2815 nm (black balls) and (b) 1531 nm (black balls) and 1023 nm (blue balls) of erbium ions (20 at%) in the LuGG garnet crystal on a semi-logarithmic scale. As usual, each temporal trace of these mid-IR or NIR emissions follows an exponential

function. The solid red lines represent the fitting results of an exponential trial function. The fit gives a time constant $\tau_f = 500 \pm 50$, 2900 ± 200 , and $480 \pm 50 \mu\text{s}$ for the emissions at 2815, 1531, and 1023 nm, respectively.

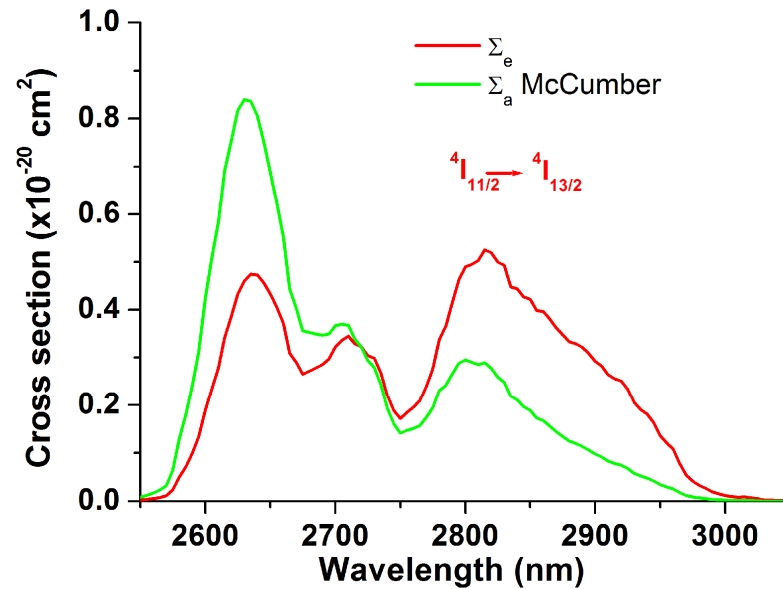


Figure 6. Mid-IR ECS (red) and ACS (green) spectra of ${}^4I_{11/2} \leftrightarrow {}^4I_{13/2}$ of erbium(20 at%)-doped LuGG crystal.

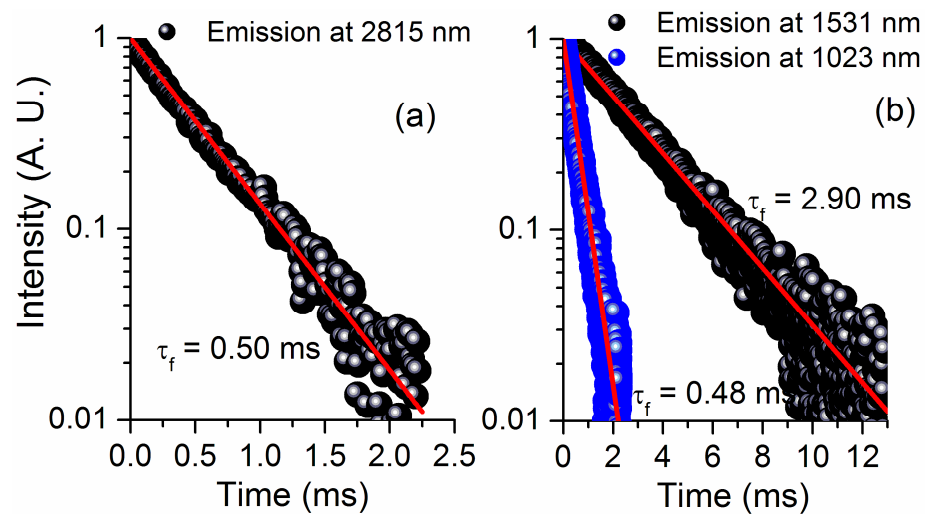


Figure 7. Transient decaying curves of NIR or mid-IR emissions at (a) 1023 (blue balls), 1531 (black balls), and (b) 2815 nm (black balls) of erbium ions (20 at%) in LuGG garnet crystal. The red solid lines represent the fitting results of a mono-exponential trial function.

For the two 980-nm-excited Vis emissions at 0.554 and 0.67 μm , however, their temporal traces do not obey an exponential profile but show considerable non-exponential behavior. Figure 8a shows the temporal decays of green (green symbols) and red (red symbols) fluorescence at 0.554 μm (${}^4S_{3/2} \rightarrow {}^4I_{15/2}$) and 0.67 μm (${}^4F_{9/2} \rightarrow {}^4I_{15/2}$) of erbium-ion in the LuGG crystal, respectively. It can be seen that both decay plots show considerable non-exponential characteristics. Rough estimations give a time constant (@1/e intensity) of $60 \pm 3 \mu\text{s}$ for the 0.554 μm fluorescence and $226 \pm 10 \mu\text{s}$ for the 0.67 μm fluorescence.

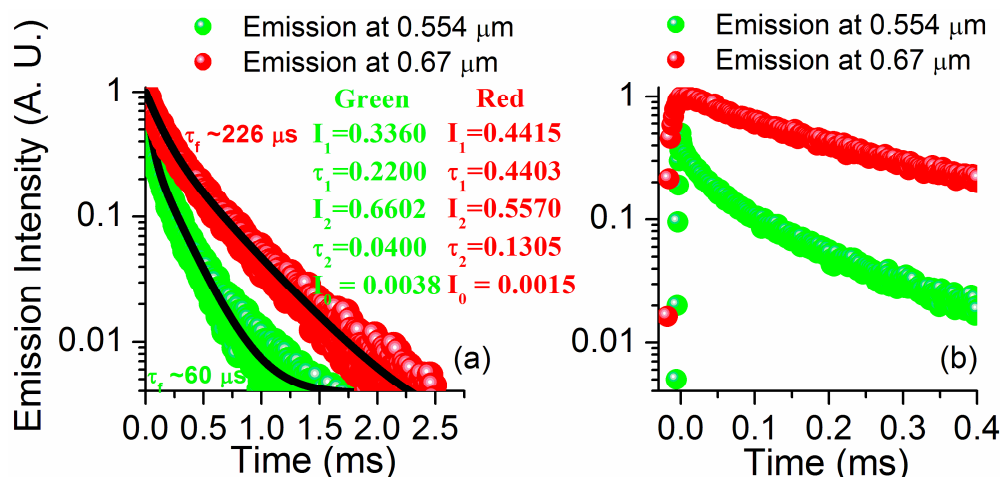


Figure 8. (a) Temporal plots of 0.98- μm -excited fluorescence of the 0.554 μm (green balls) and 0.67 μm (red balls) processes of erbium(20 at%)-doped LuGG. Black plots represent the best fits utilizing the trial function suggested by expression (5). The parameter values used for the fit are presented. (b) Two transient plots in the initial excitation-decay stage ($t \approx 0$).

A similar non-exponential temporal characteristic was also observed for erbium-doped lithium niobate crystal [26]. The temporal decay is contributed by two different types of energetic lattice points occupied by erbium ions. One type of lattice point is occupied by the erbium ions in the isolated state and another by those erbium ions in the cluster state [27,28]. Those erbium ions that are present in the crystal in the form of cluster states result in a non-exponentially decaying characteristic. The presence of clustered erbium ions enables non-radiative upconversion depopulation through cross-relaxation of inter-ionic short-distance resonant energy transfer between the erbium ions in the cluster state. The non-radiative depopulation gives rise to an additional contribution to decay and hence a non-exponential temporal characteristic. However, non-radiative cross-relaxation hardly takes place for the erbium ions in an isolated state. The relevant mathematical model is described as follows: At time t , the measured temporal fluorescence intensity, named $I(t)$, can be expressed as a double-exponential trial function, given by:

$$I(t) = I_1 \exp\left(-\frac{t}{\tau_1}\right) + I_2 \exp\left(-\frac{t}{\tau_2}\right) + I_0 \tag{5}$$

The measured temporal intensity $I(t)$ is mainly due to two types of differently energetic lattice points. The first term, with an amplitude I_1 and a lifetime parameter τ_1 , represents the contribution of erbium-ions in the isolated state; the second term, with an amplitude I_2 and a lifetime parameter τ_2 , denotes the contribution of erbium-ions in the cluster state; and the third term, I_0 , reflects the background noise. Assume that $I(t = 0) = I_1 + I_2 + I_0 = 1$.

The two temporal traces in Figure 8a were fitted using Equation (5). The best fits are shown by black curves, and the relevant fitting parameters are presented. We note that the values of τ_1 and τ_2 are 220 ± 5 and 40 ± 2 μs for the green fluorescence at 0.554 μm and 440 ± 8 and 130 ± 3 μs for the red fluorescence at 0.67 μm . The ground I_0 is below 0.4% and ignorable. The values of I_1 and I_2 are $(34 \pm 5)\%$ and $(66 \pm 10)\%$, respectively, for the green fluorescence at 0.554 μm and $(44.0 \pm 7)\%$ and $(56.0 \pm 8)\%$, respectively, for the red fluorescence at 0.67 μm . It can be seen that the I_1 (I_2) value of the 0.554 μm fluorescence may be thought to be identical to that of the 0.67 μm fluorescence within the incertitude.

The amplitude parameters I_1 and I_2 reflect the initial ($t = 0$) amplitude fractions with regard to the isolated erbium ions and the ones in the cluster state, respectively. Both are associated with respective concentrations, named C_i for the isolated erbium ions and C_c for those ones in the cluster state, because the fluorescence intensity is usually proportional to the active ion concentration (before the concentration quenching effect happens). As $I(t = 0) = I_1 + I_2 + I_0 = 1$ and $C_i + C_c = C_{\text{Er}} = 20$ at%, the value of I_1 (I_2) reflects the

concentration fraction of the erbium ions in the isolated (clustered) state in the crystal. The I_1 and I_2 values given above show that the erbium-ion presence in the studied crystal is about 40% in the isolated state and about 60% in the cluster state. As demonstrated above, either I_1 or I_2 has the same values for both emissions at 0.554 and 0.67 μm . The same I_1 or I_2 values of the two emissions give consistent results for concentration fractions of erbium ions in the isolated and clustered states in the LuGG crystal studied. This is expected. A quite high concentration of erbium-ion dopants in the crystal, $\sim 20\%$ ($\sim 3.0 \times 10^{21}$ ions/ cm^3), is the main reason why the concentration fraction of erbium-ions in the cluster state is high. The higher the erbium-ion concentration is, the smaller the distance to the adjacent erbium-ion is, and hence the larger the concentration fraction of erbium-ion in the cluster state is. In general, higher concentrations of erbium ions in the cluster state give rise to an increase in non-radiative depopulation through short-distance cross-relaxation between erbium ions in the cluster state and result in the weakening of CU and ESA processes. However, the validity of such a statement for the crystal studied here needs to be verified by additional experimental results for the following two reasons: First, depending on erbium concentration and hence inter-ion distance, there would be a competition between energy transfer and non-radiative processes. Second, the cluster structures are complicated in most cases. One cannot draw an affirmative conclusion on the basis of just an individual result. Moreover, in some crystals, the clustered ions are more likely to have formed at a lower doping level [29,30]. To make the issues clear, a concentration-dependent characterization is essential in future research.

In addition, in Figure 8b, we show the situation of the two transient plots in the initial excitation-decay stage ($t \approx 0$). We can see that the two transient plots exhibit an extended rise time before decay happens. It means that the energy transfer CU would be more likely for the excitation of the $^2\text{H}_{11/2}$ and $^4\text{S}_{3/2}$ states in the studied crystal.

Finally, it is worthwhile to point out that the erbium-doped LuGG crystal may also find its application in photovoltaics based on spectral conversion [31,32], besides the ones in the fields of display, laser, and thermal sensing mentioned in the introduction part. Future work aims to demonstrate the application.

4. Conclusions

An erbium-doped LuGG crystal has been grown, and the ECS, ACS, and temporal features of the erbium ion in the crystal have been demonstrated. The ECS spectrum is computed from the acquired emission spectrum, and the ACS spectrum is computed from the ECS spectrum based on McCumber expression as well as directly from the acquired absorption spectrum. Two approaches give consistent results for ACS spectra. The consistency implies that both approaches are correct and the results obtained from them are sound.

Investigation of the temporal dynamic characteristics of Vis, NIR, and mid-IR fluorescence reveals that both the NIR and mid-IR emissions at 1.023, 1.531, and 2.815 μm obey a single exponential profile. Instead, both green and red emissions follow a well-defined double-exponential function, with one component correlating with the erbium ions in the isolated state and another component relating to those erbium ions in the cluster state. The double-exponential temporal behavior is correlated with those erbium-ions present in the form of cluster states in the crystal, which cause non-radiative depopulation and thereby extra contributions to temporal decay via cross-relaxation of resonance between adjacent erbium-ions in the cluster state. The cross-relaxation has a small occurrence possibility for those erbium ions in the isolated state instead. A rough estimation reveals that about half of the erbium ions are present in the cluster state in the studied crystal as a result of the high doping concentration. Energy transfer CU would be more likely for the excitation of the $^2\text{H}_{11/2}$ and $^4\text{S}_{3/2}$ states in the studied crystal.

Author Contributions: P.Z.: Investigation, Writing—original draft preparation, Funding acquisition; D.-L.Z.: Conceptualization; Writing—review and editing; Supervision; Project administration; Y.W.: Validation; Resources; Writing—review and editing. All authors have read and agreed to the published version of the manuscript.

Funding: This research was funded by the National Natural Science Foundation of China under Project no. 61875148 and by the Key Program of Tianjin Sino-German University of Applied Sciences, China, under Project no. zdk2019-002.

Institutional Review Board Statement: Not applicable.

Informed Consent Statement: Not applicable.

Data Availability Statement: Not applicable.

Acknowledgments: This work was supported by the National Natural Science Foundation of China under Project no. 61875148 and by the Key Program of Tianjin Sino-German University of Applied Sciences, China, under Project no. zdk2019-002.

Conflicts of Interest: The authors declare no conflict of interest.

References

1. You, Z.; Li, J.; Wang, Y.; Chen, H.; Zhu, Z.; Tu, C.Y. Spectroscopic and laser properties of Er:LuGG crystal at ~ 2.8 μm . *Appl. Phys. Exp.* **2019**, *12*, 052019. [[CrossRef](#)]
2. Liu, M.-H.; Shao, Y.-X.; Piao, R.-Q.; Zhang, D.-L.; Wang, Y. Sellmeier dispersion and spectroscopic properties of Er³⁺-doped lutetium gallium garnet single crystal. *Results Phys.* **2021**, *30*, 104876. [[CrossRef](#)]
3. Venkatramu, V.; Giarola, M.; Mariotto, G.; Enzo, S.; Polizzi, S.; Jayasankar, C.K.; Piccinelli, F.; Bettinelli, M.; Speghini, A. Nanocrystalline lanthanide-doped Lu₃Ga₅O₁₂ garnets: Interesting materials for light-emitting devices. *Nanotechnology* **2010**, *21*, 175703. [[CrossRef](#)] [[PubMed](#)]
4. Venkatramu, V.; Falcomer, D.; Speghini, A.; Bettinelli, M.; Jayasankar, C. Synthesis and luminescence properties of Er³⁺-doped Lu₃Ga₅O₁₂ nanocrystals. *J. Lumin.* **2010**, *128*, 811–813. [[CrossRef](#)]
5. Rathaiiah, M.; Haritha, P.; Linganna, K.; Monteseuro, V.; Martín, I.R.; Lozano-Gorrín, A.D.; Babu, P.; Jayasankar, C.K.; Lavín, V.; Venkatramu, V. Infrared-to-Visible Light Conversion in Er³⁺-Yb³⁺:Lu₃Ga₅O₁₂ Nanogarnets. *Chem. Phys. Chem.* **2015**, *16*, 3928–3936. [[CrossRef](#)] [[PubMed](#)]
6. Wu, K.; Hao, L.; Zhang, H.; Yu, H.; Wang, Y.; Wang, J.; Tian, X.; Zhou, Z.; Liu, J.; Boughton, R.I. Lu₃Ga₅O₁₂ crystal: Exploration of new laser host material for the ytterbium ion. *J. Opt. Soc. Am. B* **2012**, *29*, 2320–2328. [[CrossRef](#)]
7. Han, W.J.; Ma, Y.J.; Dou, X.D.; Wang, L.S.; Xu, H.H.; Liu, J.H. Passive Q-switching laser properties of Yb:Re₃Ga₅O₁₂ (Re = Y, Lu, Gd) garnets with GaAs semiconductor saturable absorber. *Opt. Commun.* **2018**, *423*, 1–5. [[CrossRef](#)]
8. Serres, J.M.; Loiko, P.; Mateos, X.; Yu, H.H.; Zhang, H.J.; Liu, J.H.; Yumashev, K.; Griebner, U.; Petrov, V.; Aguilo, M.; et al. Q-switching of Yb:YGG, Yb:LuGG and Yb:CNGG lasers by a graphene saturable absorber. *Opt. Quant. Electron.* **2016**, *48*, 197. [[CrossRef](#)]
9. Han, W.; Wu, K.; Tian, X.; Xia, L.; Zhang, H.; Liu, J. Laser performance of ytterbium-doped gallium garnets: Yb:Re₃Ga₅O₁₂ (Re = Y, Gd, Lu). *Opt. Mater. Express* **2013**, *3*, 920–927. [[CrossRef](#)]
10. Liu, J.; Tian, X.; Zhou, Z.; Wu, K.; Han, W.; Zhang, H. Efficient laser operation of Yb:Lu₃Ga₅O₁₂ garnet crystal. *Opt. Lett.* **2012**, *37*, 2388–2390. [[CrossRef](#)]
11. He, J.; Mei, Y.; Zheng, W.-C.; Liu, H.-G. Thermal shifts and electron-phonon coupling parameters for Cr³⁺-doped Lu₃Al₅O₁₂ and Lu₃Ga₅O₁₂ garnet crystals. *Optik* **2018**, *171*, 304–307. [[CrossRef](#)]
12. Haritha, P.; Viswanath, C.D.; Linganna, K.; Babu, P.; Jayasankar, C.; Lavín, V.; Venkatramu, V. Nanocrystalline Sm³⁺-doped Lu₃Ga₅O₁₂ garnets: An intense orange-reddish luminescent material for white light emitting devices. *J. Lumin.* **2016**, *179*, 533–538. [[CrossRef](#)]
13. Sun, G.; Zhang, Q.; Yang, H.; Luo, J.; Sun, D.; Gu, C.; Yin, S. Crystal growth and characterization of Ho-doped Lu₃Ga₅O₁₂ for 2 μm laser. *Mater. Chem. Phys.* **2013**, *138*, 162–166. [[CrossRef](#)]
14. Wu, K.; Yao, B.; Zhang, H.; Yu, H.; Wang, Z.; Wang, J.; Jiang, M. Growth and properties of Nd:Lu₃Ga₅O₁₂ laser crystal by floating-zone method. *J. Cryst. Growth* **2010**, *312*, 3631–3636. [[CrossRef](#)]
15. Novoselov, A.; Yoshikawa, A.; Nikl, M.; Pejchal, J.; Fukuda, T. Study on crystal growth and scintillating properties of Bi-doped Lu₃Ga₅O₁₂. *J. Cryst. Growth* **2006**, *292*, 236–238. [[CrossRef](#)]
16. Lifante, G.; Núñez, L.; Cussó, F. Polarization effects on the line-strength calculations of Er³⁺-doped LiNbO₃. *Appl. Phys. B Laser Opt.* **1996**, *62*, 485–491. [[CrossRef](#)]
17. Miniscalco, W.J.; Quimby, R.S. General procedure for the analysis of Er³⁺ cross sections. *Opt. Lett.* **1991**, *16*, 258–260. [[CrossRef](#)]
18. Martin, R.M.; Quimby, R.S. Experimental evidence of the validity of the McCumber theory relating emission and absorption for rare-earth glasses. *J. Opt. Soc. Am. B* **2006**, *23*, 1770–1775. [[CrossRef](#)]
19. Moulton, P.F. Spectroscopic and laser characteristics of Ti:Al₂O₃. *J. Opt. Soc. Am. B* **1986**, *3*, 125–133. [[CrossRef](#)]

20. Eggleston, J.; DeShazer, L.; Kangas, K. Characteristics and kinetics of laser-pumped Ti:sapphire oscillators. *IEEE J. Quantum Electron.* **1988**, *24*, 1009–1015. [[CrossRef](#)]
21. Pernas, P.L.; Cantelar, E. Emission and Absorption Cross-Section Calculation of Rare Earth Doped Materials for Applications to Integrated Optic Devices. *Phys. Scr.* **2005**, *2005*, 93. [[CrossRef](#)]
22. McCumber, D.E. Theory of Phonon-Terminated Optical Masers. *Phys. Rev.* **1964**, *134*, A299–A306. [[CrossRef](#)]
23. Lazaro, J.; Valles, J.; Rebolledo, M. In situ measurement of absorption and emission cross sections in Er/sup 3+/-doped waveguides for transitions involving thermalized states. *IEEE J. Quantum Electron.* **1999**, *35*, 827–831. [[CrossRef](#)]
24. Rebolledo, M.A.; Vallés, J.A.; Setién, S. In situ measurement of polarization-resolved emission and absorption cross-sections of Er-doped Ti:LiNbO₃ waveguides. *J. Opt. Soc. Am. B* **2002**, *19*, 1516–1520. [[CrossRef](#)]
25. Lazaro, J.A.; Valles, J.A.; Rebolledo, M.A. Determination of emission and absorption cross-sections of Er³⁺ in Ti:LiNbO₃ waveguides from transversal fluorescence spectra. *Pure Appl. Opt.* **1998**, *7*, 1363–1371. [[CrossRef](#)]
26. Ju, J.J.; Lee, M.-H.; Cha, M.; Seo, H.J. Energy transfer in clustered sites of Er³⁺ ions in LiNbO₃ crystals. *J. Opt. Soc. Am. B* **2003**, *20*, 1990–1995. [[CrossRef](#)]
27. Gill, D.M.; McCaughan, L.; Wright, J.C. Spectroscopic site determinations in erbium-doped lithium niobate. *Phys. Rev. B* **1996**, *53*, 2334–2344. [[CrossRef](#)]
28. Dierolf, V.; Koerdts, M. Combined excitation-emission spectroscopy of Er³⁺ ions in stoichiometric LiNbO₃: The site selectivity of direct and up conversion excitation processes. *Phys. Rev. B* **2000**, *61*, 8043–8052. [[CrossRef](#)]
29. Catlow, C.R.A.; Chadwick, A.V.; Greaves, G.N.; Moroney, L.M. Direct observations of the dopant environment in fluorites using EXAFS. *Nature* **1984**, *312*, 601–604. [[CrossRef](#)]
30. Petit, V.; Camy, P.; Doualan, J.L.; Portier, X.; Moncorgé, R. Spectroscopy of Yb³⁺:CaF₂: From isolated centers to clusters. *Phys. Rev. B* **2008**, *78*, 085131. [[CrossRef](#)]
31. Arnaoutakis, G.E.; Favilla, E.; Tonelli, M.; Richards, B.S. Single crystal monolithic upconverter solar cell device tandems with integrated optics. *J. Opt. Soc. Am. B* **2022**, *39*, 239–247. [[CrossRef](#)]
32. Boccolini, A.; Favilla, E.; Tonelli, M.; Richards, B.S.; Thomson, R.R. Highly efficient upconversion in Er³⁺ doped BaY₂F₈ single crystals: Dependence of quantum yield on excitation wavelength and thickness. *Opt. Express* **2015**, *23*, A903–A915. [[CrossRef](#)]

Disclaimer/Publisher’s Note: The statements, opinions and data contained in all publications are solely those of the individual author(s) and contributor(s) and not of MDPI and/or the editor(s). MDPI and/or the editor(s) disclaim responsibility for any injury to people or property resulting from any ideas, methods, instructions or products referred to in the content.